Multilevel Composition: A new method for revealing complex geological features in three-dimensional seismic reflection data

Muhedeen A. Lawal [a], Ingo Pecher [b,c], Or.M. Bialik [a,d], Nicolas D. Waldmann [a], Jörg Bialas [e], Zvi Koren [f,g], Yizhaq Makovsky [a,h,*]

[a] *Dr. Moses Strauss Department of Marine Geosciences, Charney School of Marine Sciences (CSMS), University of Haifa, Haifa, 3498838, Israel*
[b] *Department of Physical and Environmental Sciences, Texas A&M University, Corpus Christi, TX 78412, USA*
[c] *School of Environment, University of Auckland, Auckland, 1142, New Zealand*
[d] *Department of Geosciences, University of Malta, Msida, MSD 2080, Malta*
[e] *Marine Geodynamics, GEOMAR Helmholtz Centre for Ocean Research Kiel, 24148, Kiel, Germany*
[f] *AspenTech, Gav-Yam, Herzeliya, 46120, Israel*
[g] *Department of Geophysics, Tel Aviv University, Tel Aviv, Israel*
[h] *Hatter Department of Marine Technologies, CSMS, University of Haifa, Haifa, 3498838, Israel*

ARTICLE INFO

ABSTRACT

Advanced seismic data and multi-attribute visualization techniques, such as color blending of attributes, have considerably enhanced the capability of interpreters to characterize geological features in three-dimensional (3D) seismic reflection datasets. However, high resolution investigation of complex, vertically linked geological features such as channel systems and fluid conduits, remains challenging. These features may appear in the dataset as pronounced attribute anomalies, such as high-amplitude or spectrally or structurally enhanced seismic reflectivity bands, at several depth levels. Vertical linkages between these features, however, may not be readily established. We have developed an innovative method, Multilevel Composition, for an intuitive display of vertically connected features. Our method involves the composition of attribute maps from three different depth/time windows or slices onto a single map, in which inter-window/layer depth information is coded in colors. Multilevel Composition starts with the identification of suitable seismic attributes, such as high amplitudes in the examples displayed here, to map features of geological interest. At least one reference horizon is then identified and mapped in the vicinity of the target window of interest. Three sub-windows are then defined with respect to the reference horizon(s) based on the vertical and spatial distribution of the geological features. Relevant seismic attributes are computed for each of the sub-windows, and the resulting maps, one from each sub-window, are assigned basic color channels and are co-rendered to reveal multilevel linkages between these features. We demonstrate the efficacy of this method by applying it to two 3D seismic datasets, one illuminating deep-water depositional elements in the eastern Nile fan, eastern Mediterranean and the other targeting seafloor seeps and underlying gas migration systems beneath the Omakere Ridge, offshore New Zealand. The new method is simple and should be easy to implement to enhance seismic interpretation workflows.

1. Advances in seismic interpretation techniques

Unravelling the huge amount of information contained in seismic reflection images is the main goal of seismic interpretation (Bacon et al., 2010; Brown, 1991). The aim of such task is to obtain in-depth understanding of the subsurface geology and to build detailed structural/stratigraphic models. In recent years, seismic interpretation capabilities have seen remarkable improvements, many of which have become possible due to the development of a wide range of volumetric seismic attributes (Brown, 1991; Chopra and Marfurt, 2006, 2007).

These generally form a key part of integrated seismic interpretation workflows. Different types of seismic attributes have been designed to enhance specific geological characteristics within the seismic images (Brown, 2001; Chopra and Marfurt, 2007). Useful geological information can be visualized through two-dimensional (2D), map-based attribute displays, preferably through high fidelity 3D multi-attribute display techniques such as color blending (Henderson et al., 2008), volume rendering (Alves et al., 2015; Chaves et al., 2011) and geobody extraction (Chaves et al., 2011).

Color blending makes it possible to create multi-attribute displays with greater clarity and detail than simple monochromatic attribute displays. This utilizes properties of end member addition across color space using red-green-blue (RGB), hue-saturation-value (HSV), cyan-magenta-yellow (CMY) or other color models. Volumetric co-rendering of multiple attributes, and particularly using the RGB color model, is widely used to visualize subsurface geological features (Henderson et al., 2008; Stark, 2006). A common use is in the co-rendering of frequency volumes derived from spectral decomposition (Partyka et al., 1999). The use of color blending for geological visualization has been conventionally limited to volume-based attribute displays.

Many geological features, including channels, mass transport deposits, reservoirs and seeps (and their underlying features), are stacked vertically and occur across multiple levels/windows (i.e. multilevel features) in a seismic dataset. Conventionally, the characterization of these features in seismic reflection data is done through volume-visualization, the creation of attribute maps of each window/level, slices, section displays and transparency or overlays to see how the features compare in depth or vertically (Koren and Ravve, 2011; Kumar et al., 2021; Kumar and Sain, 2020; Safadi et al., 2017). These approaches may not always be sufficiently helpful, to establish the connections between the investigated multi-level features and their interpretation.

Proper visualization and characterization of these geological features could be particularly challenging when (1) there are no continuous and easy-to-interpret horizons around the features; or (2) the seismic attributes, resulting from the multiple levels where the features occur, are to be presented in a single, intuitive map. To resolve this difficulty, we propose a method that enhances the visualization of geological features from three depth or time intervals at the same time, by incorporating them into a single map. We demonstrate the advantages of this method in enriching the visualization and interpretability of fine multilevel structural and stratigraphic features.

This paper describes a method to enhance the visualization of multilevel geological features using their composed or blended attributes. This method, which we name "Multilevel Composition", provides co-rendered versions of multilevel attribute maps, and is shown here to be an effective visualization and characterization approach in the seismic interpretation workflow. This paper starts with a methodology section, followed by two case studies that use 3D seismic data to investigate (a) deep-water depositional elements of the eastern fan of the Nile in the Levant Basin, eastern Mediterranean and (b) seafloor cold seeps from the Omakere Ridge, offshore New Zealand.

2. Datasets

The first application presented here of the Multilevel Composition method is based on the western half of the Sara-Myra 3D seismic data from the eastern deep-sea fan of the Nile at water depths of ~1100 m–~1500 m in the Levant Basin (Fig. 1a). Technical details of the dataset are available from Table 1. Processing procedures applied to the data include band pass filtering, diffraction-multiples removal, normal move-out correction, fold normalization, spatial anti alias filtering, amplitude preservation techniques, and 3D Kirchhoff pre-stack depth migration. Such a processing sequence is an industry-standard for amplitude preserving imaging, though not rigorously "true amplitude". The second case study is on a 3D seismic image from a high-resolution P-cable 3D seismic dataset, acquired over an area of 2 km × 7 km on the Omakere Ridge on the Hikurangi Margin east of New Zealand (Fig. 1b). The dataset was acquired using sixteen streamers at 10 m spacing and a 4.2 L GI-gun deployed at 2 m water depth (Table 1). The processing procedures applied to the data include CMP binning, band pass filtering, deconvolution to attenuate seafloor ghosts, tide and residual static corrections, amplitude preservation and 3D Kirchhoff time migration (Plaza-Faverola et al., 2014). The datasets analyses were carried out in the depth (meters) domain for the Sara-Myra dataset and in vertical two-way traveltime (milliseconds) for the Omakere dataset, using AspenTech's Subsurface Science and Engineering (SSE) software. This software package includes advanced color blending capabilities.
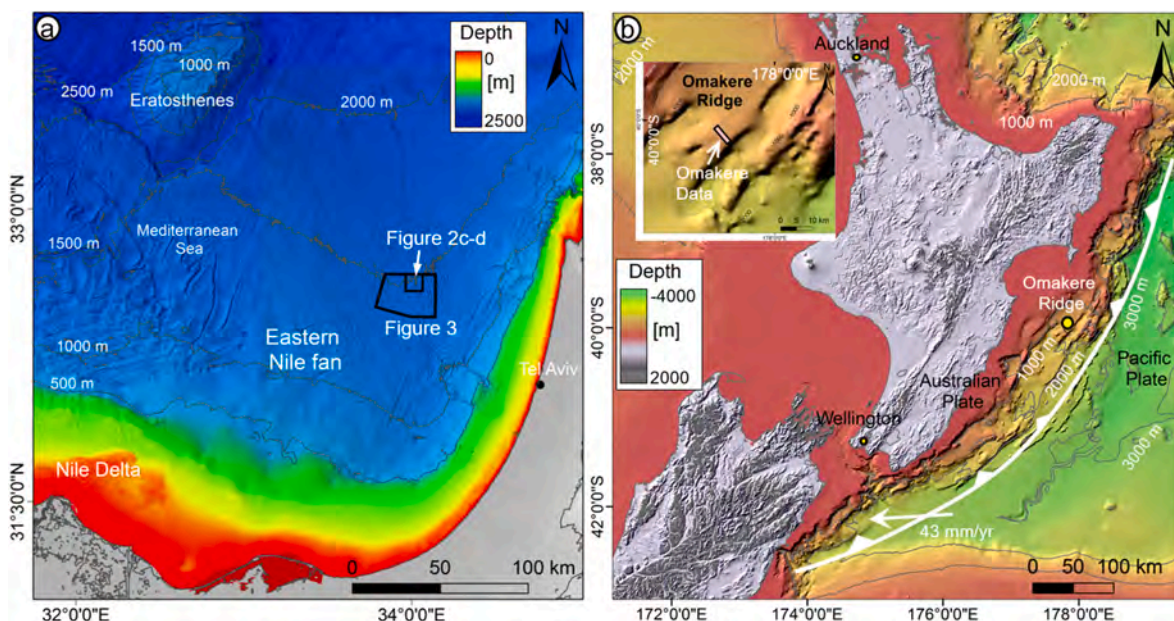

Fig. 1. Bathymetry of the study areas. (a) The eastern deep-sea fan of the Nile river in the eastern Mediterranean (from EMODNET: https://portal.emodnet-bathy metry.eu/ and GEBCO: https://download.gebco.net/), overlaid with the outline of the Sara-Myra 3D seismic data. (b) Omakere Ridge, offshore New Zealand (from NIWA: https://niwa.co.nz/our-science/oceans/bathymetry), overlaid with the outline of the Omakere 3D seismic data.

Table 1
Technical details of the datasets used in this study.

Survey name	Acquisition details	Survey type and unit	Imaging details	Waveform and display
Sara-Myra	Acquired by CGG-Veritas Year: 2001	Industry standard Depth Migrated 3D Seismic reflection, Depth in meters	Bin size: 6.25 m × 25 m Sampling interval: 2 ms Inline and Crossline spacing: 25 m and 12.5 m Vertical and horizontal resolution: ~10 m	Zero phase Display: Society of Exploration Geophysicists (SEG) Normal Polarity convention.
Omakere	Acquired during SO-214 cruise Year: 2011	P-Cable Time Migrated 3D Seismic reflection, TWT seconds	Bin size: 6.25 m × 6.25 m Sampling interval: 0.25 ms Inline and Crossline spacing: 6.2 m and 6.2 m Vertical and lateral resolution: ~6.25 m	Zero phase Display: SEG Normal Polarity convention.

3. The Multilevel Composition method

3.1. Attribute selection and expression

Seismic attributes refer to quantitative measures of certain characteristics of a seismic dataset and are used to enhance geological or geophysical interpretation of the subsurface (Brown, 2001; Chopra and Marfurt, 2007). Signal envelope, root mean square (RMS) amplitude and maximum positive amplitude are some of the most basic attributes used by seismic interpreters and are used in this paper to demonstrate the Multilevel Composition method. The signal envelope or reflection strength attribute represents the instantaneous energy of the seismic signal (Chopra and Marfurt, 2005). It generates only positive amplitudes and is commonly used for revealing changes in deposition and lithology, tuning effects and sequence boundaries (Subrahmanyam and Rao, 2008). In this study, signal-envelope maps extracted from the Sara-Myra dataset are used to delineate buried depositional features such as leveed-channels and crevasse splays (Figs. 2–4).

The maximum positive amplitude is the peak amplitude of the positive portion of the seismic trace. Hence, it is suitable for delineating features that are characterized by positive amplitudes (Chopra and Marfurt, 2007) such as authigenic carbonates, shell debris and gas hydrates typically associated with seafloor seepage (Judd and Hovland, 2007; Roberts et al., 2006). Consequently, maximum positive amplitude attribute maps were extracted from the Omakere 3D seismic data (Fig. 5) to delineate seafloor seeps and sub-seafloor seepage-related features (Figs. 6 and 7). Furthermore, the RMS amplitude is computed as the square root of the sum of the squared amplitudes divided by the number of samples. As RMS amplitudes combine the effect of both positive and negative amplitudes, they are suitable for fluids analysis (Brown, 1991). In this study, RMS amplitude maps from the Omakere dataset are used to reveal the distribution of subsurface gas-bearing intervals (Figs. 8 and 9).

3.2. Color blending

Color models like the RGB, HSV and CMY are color spaces where the color is defined by a 3D coordinate system, based on specific spectral windows along the visual spectrum (Al-Shuhail et al., 2017; Cao et al., 2016; Marfurt, 2015). Here we chose the commonly used RGB color blending approach, an additive color model that intermixes the three primary colors red, green and blue, to produce secondary colors. Each color component (or channel) in the RGB model is represented by 8 bits, producing a blend with a color depth of 24 bits or 16,777,216 colors. Secondary colors, including white, cyan, yellow and magenta, depend on the intensity of each primary color components ranging from low (0) to high (255) (Cao et al., 2015). Reliable geological interpretation requires understanding of the complex color output and the ability to separate noise from useful information.

3.3. Multilevel Composition via color blending

The selection of suitable seismic attributes for the analysis of the geologic features of interest is the first step in our workflow, and is essential for the successful Multilevel Composition application. The application of Multilevel Composition involves five steps (Fig. 2a), starting with the selection of a time or depth window of interest within a seismic image (Fig. 2a – step 1). The optimal window should contain the features of geological interest. This is followed by the selection of one or more suitable reference horizons near the chosen window for attribute computations (Fig. 2a – step 2). These horizons are ideally continuous and close enough to the features of interest, such that the features can be delineated on attribute maps that are referenced to the horizons.

Next, the selected window is divided into three sub-windows, with respect to the reference horizon(s) to enable detailed interval by interval characterization of the features (Fig. 2a – step 3). Surface or interval-based attributes that are derived from their respective attribute volumes are subsequently computed for each sub-window using the interpreted reference horizon(s) (Fig. 2a – step 4). This is followed by color assignment in which the resulting attribute maps are assigned with basic colors and are co-rendered in the combined (here RGB) color space (Fig. 2a – step 5). This is similar to the blending of spectral decomposition, where the color is assigned based on frequency. For Multilevel Composition, the colors are assigned based on the stratigraphic position or depth of the geological features of interest.

Fig. 2b presents an application of Multilevel Composition, at an interval of interest of 15–120 m below the seafloor (Fig. 2b), where the features of interest dominantly occur. However, identifying a continuous and easy-to-interpret horizon for attribute computation within this interval seems difficult. The seafloor itself was therefore selected as a reference horizon. The interval of interest was then divided into three sub-intervals/sub-windows i.e. 15–30 m (bounded by the red lines), 25–60 m (green) and 55–120 m (blue) based on the predominant vertical extent of the features of interest (Fig. 2b).

The signal envelope attribute was computed for each of the three sub-windows (Fig. 2c). This was followed by color assignment in which the resulting attribute maps were assigned to red (shallowest; 15–30 m), green (intermediate; 25–60 m), and blue (deepest; 55–120 m) colors (Fig. 2b–c). The overlap in the selection of sub-windows allows intermixing of colors, enabling more efficient illumination of multilevel linkages. Following color assignment, the maps are co-rendered (i.e., blended) and displayed in the RGB color space (Fig. 2d), with the estimated combined color scale shown to the left of Fig. 2d. Additional colors result from blending of the basic color layers. For effective color blending of computed attribute maps, such as the one in Fig. 2c–d, the intensities of the basic color channels should be balanced.

3.4. Spectral decomposition

Spectral decomposition (Partyka et al., 1999) was performed with reference to the seafloor horizon and was done within the interval of interest in this study (15–120 m below seafloor), using central frequencies of 15 Hz, 30 Hz, and 70 Hz. This was followed by color blending in the RGB color space (Figs. 3c and S1b). Spectral decomposition was carried out in this study to (a) compare its results to those
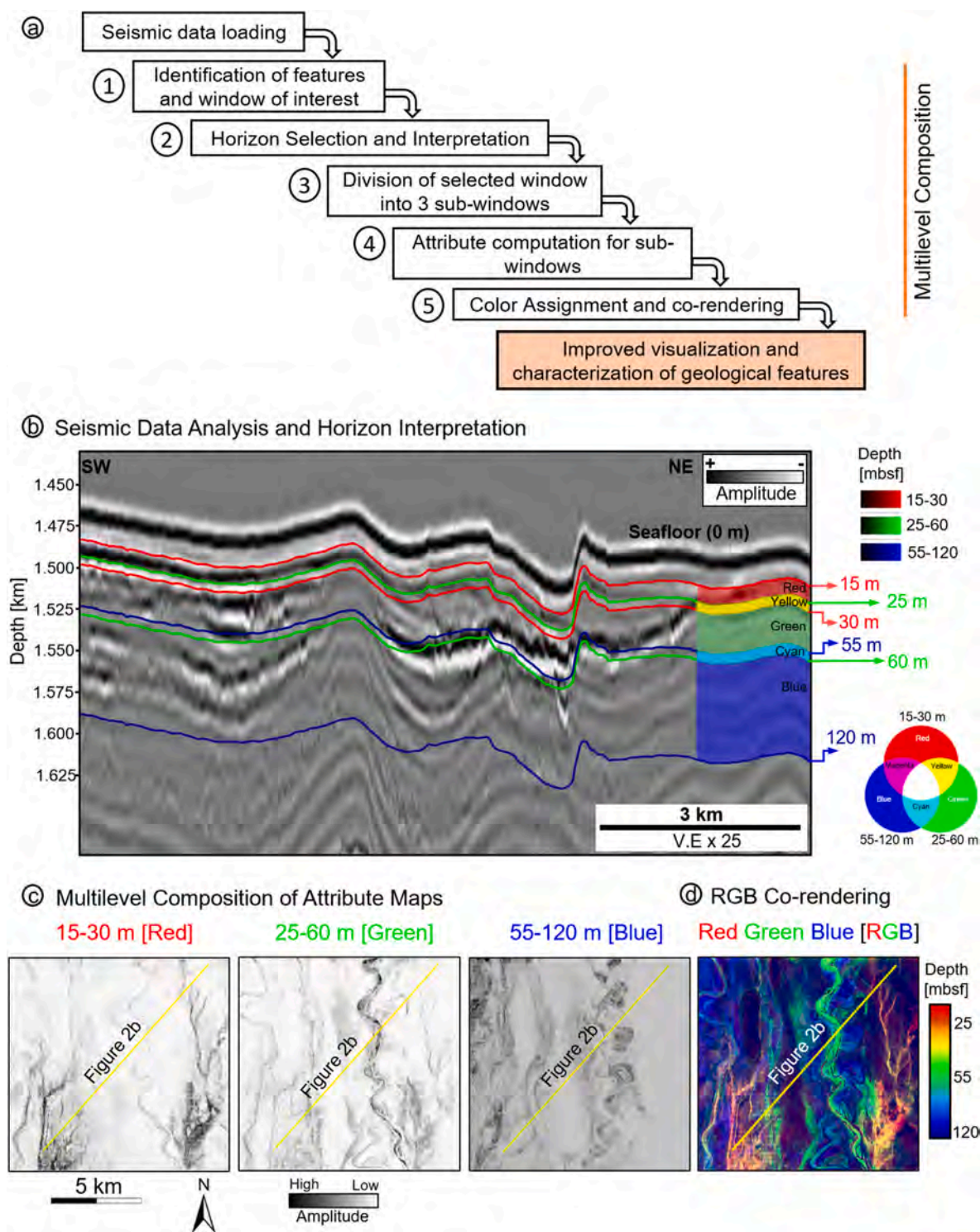
Fig. 2. (a) The multilevel composition method workflow, showing the five steps involved. (b) A depth-migrated seismic profile from the Sara-Myra 3D seismic dataset (Fig. 1a), demonstrating the attribute extraction procedure. The seafloor is used as a single reference surface. The depth interval of geological interest (15–120 m below the seafloor) is divided onto three sub-windows: 15–30 m (bounded by red lines), 25–60 m (green lines) and 55–120 m (blue lines). Attributes extracted in each of these intervals are assigned with red, green and blue colors. The colored interfaces shown on the right depict the intervals of the seismic data that are colored red, green and blue, as well as the yellow and cyan that result from the blending of the respective basic colors. (c) Signal envelope attribute maps extracted for each of the three depth intervals shown in (b), each highlighting different geological features. (d) Blending of the signal envelope maps in the RGB color space, with the attribute maps assigned red (shallowest; 15–30 m), green (intermediate; 25–60 m), and blue (deepest; 55–120 m) colors. The combined color scale (left) estimates the depth below the seafloor for the blended image colors for a signal envelope at full saturation. The profile in (b) is outlined (yellow line) in (c) and (d). (For interpretation of the references to color in this figure legend, the reader is referred to the Web version of this article.)
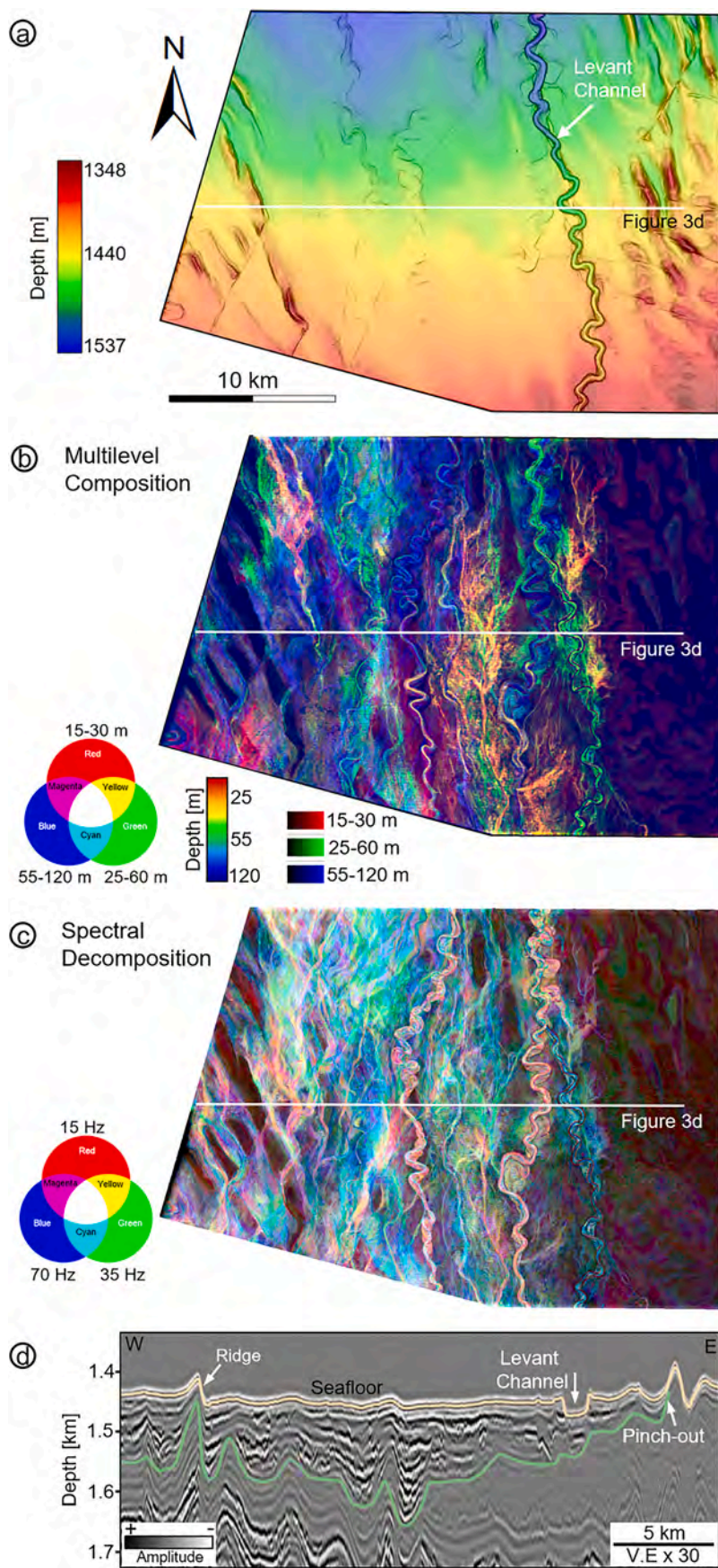
Fig. 3. (a) Bathymetry of the case study area in the eastern Nile fan in the Levant Basin, as picked from the Sara-Myra 3D seismic dataset, color-coded with water depth (right color bar) and shaded based on the bathymetric gradient. (b) A multilevel RGB composite image of signal-envelope maps, extracted from the Sara-Myra 3D seismic dataset for the 15–30 m (red), 25–60 m (green), and 55–120 m (blue) below the seafloor (bottom color coding). The middle color bar estimates the depth below the seafloor, which is reflected by the combined colors of the image. The image delineates the relative stratigraphic position of buried paleo- deep-water channels and crevasse splays and their interactions and helps to constrain the evolution of this system. (c) An RGB composite image of spectral decomposition results over the same 15–120 m interval below the seafloor, combining the 15 Hz (red), 35 Hz (green), and 70 Hz (blue) central frequency bands (color coding on the right). This image delineates the same features as in (a), color coded in relation primarily to their thickness, but offers limited information on their stratigraphic relationship, depth or their stacking pattern. (d) A W-E oriented seismic profile (white outline in a-c) showing a band of discontinuous, multilevel high amplitude sub-seafloor seismic reflectivity down to ~1.5 km below the seafloor, and which pinches-out at ridge flanks in the east and west. This reflectivity is imaged in (b) and (c) as the intricate system of buried deep-water channels and related features. (For interpretation of the references to color in this figure legend, the reader is referred to the Web version of this article.)
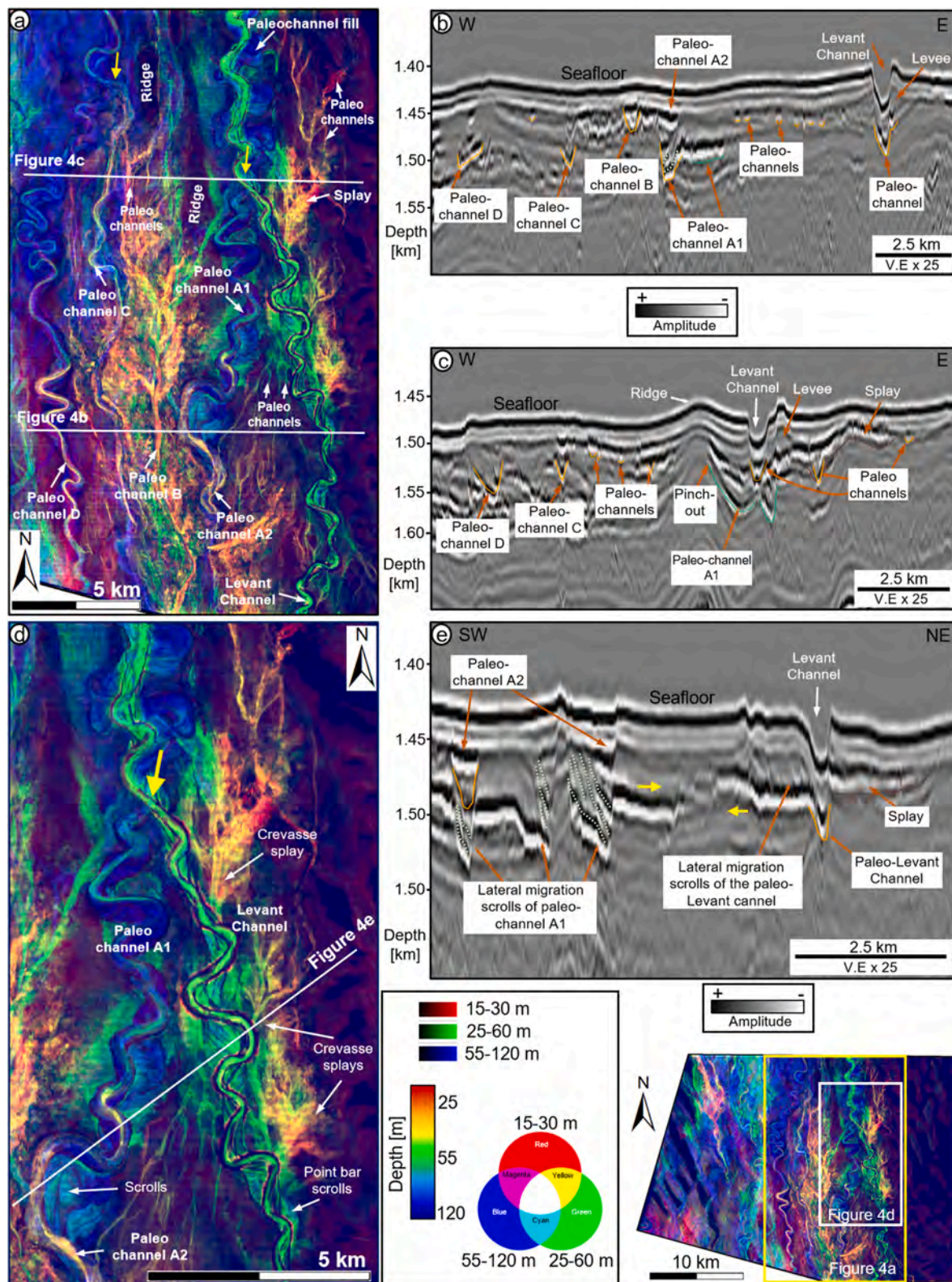
Fig. 4. (a) A zoomed part of Fig. 3b RGB multilevel composite map (see bottom right for location and color scales), highlighting multiple buried paleo depositional features (as labeled) within the study area. The colors of the different features represent their relative stratigraphic positions. (b, c) W-E oriented seismic profiles from the Sara-Myra 3D seismic dataset (outlined in white in (a)), show the different depositional elements highlighted by the Multilevel Composition in (a) in their stratigraphic context. (d) A zoomed part of (a) (see bottom right for the location and color scales) showing that the stratigraphically higher (green colored) paleo Levant channel overlaps northwards (yellow arrow) onto the track of the stratigraphically lower (blue colored) paleo channel A1. Paleo channel A2 is etched into the overburden overlaying paleo channel A1 and is stratigraphically higher than both. Note the occurrence of several scrolls indicating lateral migration of the channels. (e) A SW-NE-oriented seismic profile (outlined in white in (d)) shows the different depositional elements highlighted by the Multilevel Composition in (d) and demonstrates the difficulty in interpreting the relative stratigraphic positions of paleo channel A1 and the paleo Levant channel, a difficulty which is resolved by the Multilevel Composition in (d). (For interpretation of the references to color in this figure legend, the reader is referred to the Web version of this article.)
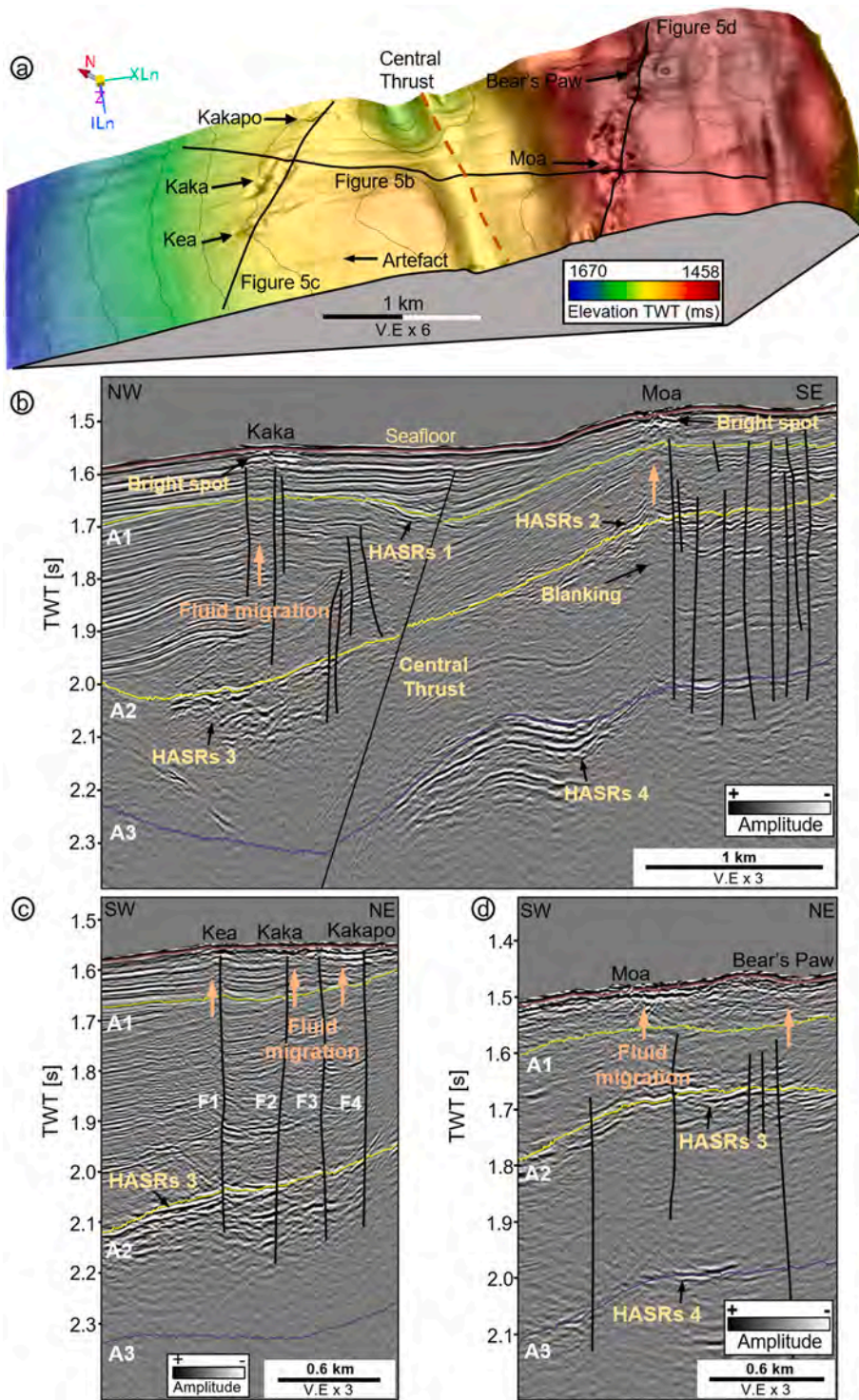
6

Fig. 5. (a) A 3D shaded relief depiction of the Omakere Ridge bathymetry (color coded by water depth), as mapped based on the Omakere 3D seismic dataset, showing two ridges separated by a trench that marks the surface projection of the central thrust fault. The morphological expressions of the Kea, Kaka and Kakapo seeps appear to the west of the central thrust fault and the Moa and Bear's Paw seeps to the east of the thrust. Black lines highlight the seismic profiles shown in (b)–(d). (b) A NW-SE seismic profile from the Omakere 3D seismic dataset, crossing the Kaka and Moa seafloor seeps and showing their underlying features. Three reference horizons, A1, A2 and A3, mapped across the dataset following Plaza-Faverola et al. (2014) are marked in green, yellow and blue, respectively. These horizons may not represent the same stratigraphic level of the two sides of the central thrust fault (black line). Also shown are localized subsurface high amplitude reflections (HASRs 1–4), sub-seep bright spots with associated underlying vertical zone of blanked seismic reflections, and a set of minor faults (black lines). (c) A NE-SW seismic profile from the Omakere 3D seismic dataset across the Kea, Kaka and kakapo seeps, showing their underlying enhanced reflections and faults (F1–F4). (d) A seismic profile from the Omakere 3D seismic dataset across the Moa and Bear's Paw seeps, showing their underlying HASRs and faults. Peach arrows indicate potential sub-vertical fluid focusing from the HASRs to the seafloor seeps. TWT[s]: Two-Way Time in Seconds. (For interpretation of the references to color in this figure legend, the reader is referred to the Web version of this article.)

derived from Multilevel Composition and (b) to verify the consistency between the two complementary methods.

4. Case study applications of Multilevel Composition

4.1. Eastern deep-sea fan of the Nile, eastern Mediterranean

The first case study area is in the eastern extension of the deep-sea fan of the Nile in the Levant Basin, eastern Mediterranean (Fig. 1a). The interval of interest in this area comprises the top of the Quaternary sedimentary section below the seafloor. It is dominated by multiple Nile-derived leveed-channels, crevasse splays, and lobe shape-based features that are buried within multiple intervals below the seafloor and interact with fold ridges (Clark and Cartwright, 2009; Folkman and Mart, 2008; Sagy et al., 2020; Tayber et al., 2019). The depositional features are multiplexed, and their sediments are deposited in a complex pattern, making it difficult to decipher their evolution. The goal of the Multilevel Composition method here was to better visualize and characterize these depositional elements, resolve their complexities and relative sequence of deposition. The method enables better understanding of the
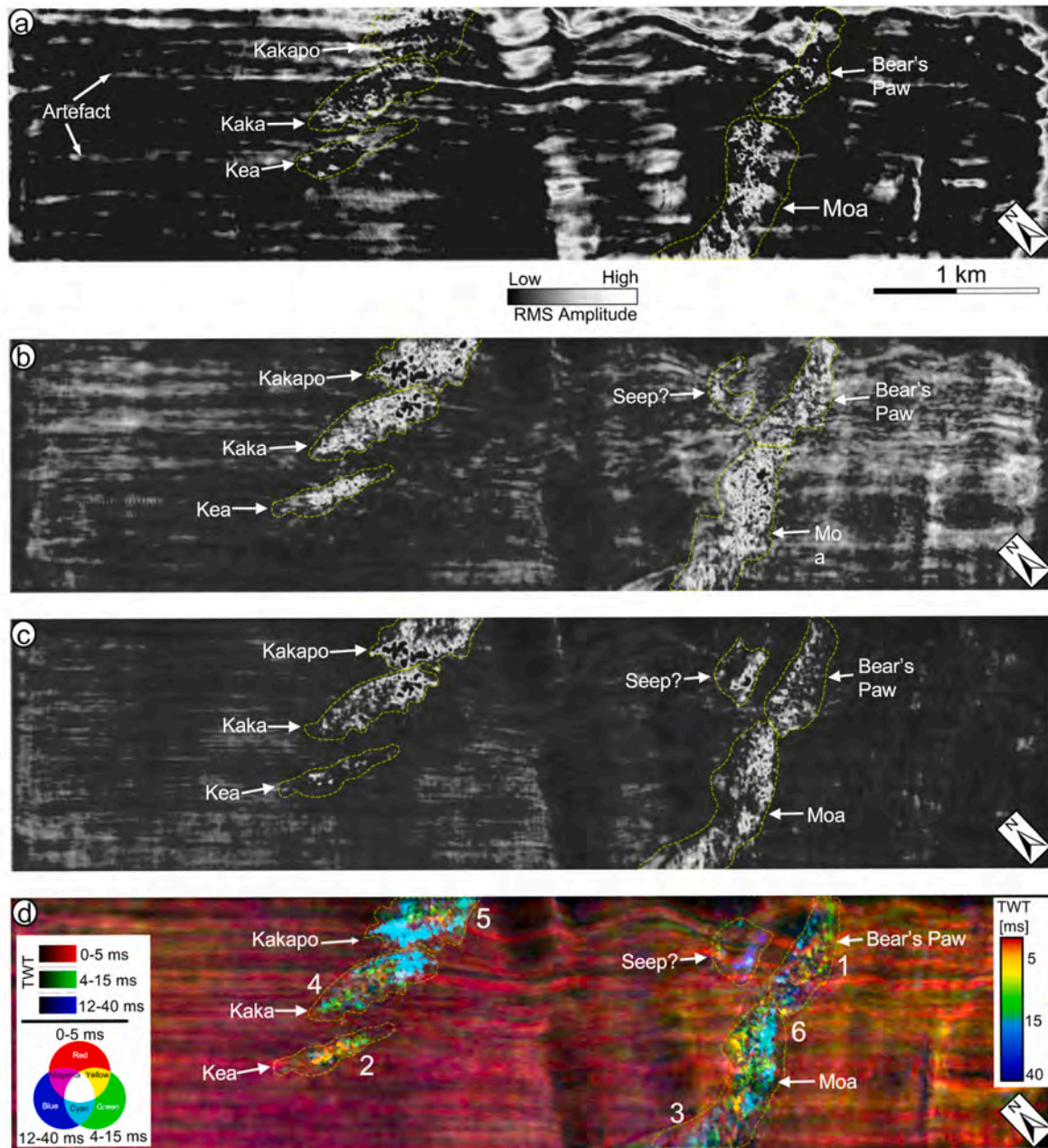
Fig. 6. (a) A maximum positive-amplitude map, extracted at 0–5 ms of the seafloor from the Omakere 3D seismic dataset, revealing localized high amplitude anomalies at the locations of the Kea, Kaka, Kakapo, Moa and Bear's Paw seeps, as well as striped acquisition artefacts. (b) A maximum positive-amplitude map, extracted at 4–15 ms below the seafloor, highlighting localized amplitude anomalies below the seafloor seeps. Note the additional localized amplitude anomaly to the north of Bear's Paw seep. (c) A maximum positive-amplitude map, extracted at 12–40 ms below the seafloor, also showing localized amplitude anomalies at the location of the seeps. Note the reduced amplitude responses at the Kea seep and the enhanced response north of the Bear's Paw site. (d) A multilevel RGB composite of the amplitude maps at (a) (0–5 ms, red), (b) (4–15 ms, green), and (c) (12–40 ms, blue), highlighting the throughout amplitude enhancement at the seeps (bright colors) and the different depth of their feeding systems (green and blue tones), as well as illuminating the anomaly to the north of the Bear's Paw seep. Numbers rank the intensity of each of the seeps (1-highest and 6-lowest) based on seafloor observations by Jones et al. (2010), which appear to be inverse of the intensities of their composed amplitude responses. Note the color scale in Fig. 6d. TWT [ms]: Two-Way time in milliseconds. (For interpretation of the references to color in this figure legend, the reader is referred to the Web version of this article.)

channel-lobe systems deposition patterns and their evolution and provides an important approach to limit interpretation time in this area. In the evaluation of the Sara-Myra seismic dataset, the geological features of interest in this study are located within 15–120 m below the seafloor. This window was further divided into three sub-windows 15–30 m, 25–60 m, and 55–120 m, based on the distribution of the channel lobe systems of interest within the intervals. The subsequent steps of the proposed method are detailed in the data and methodology section

(Fig. 2).

4.1.1. Background geology

The Quaternary in the Levant was associated with the deposition of sediments via leveed-channel and lobe systems. These sediments are buried within the uppermost ~200–250 m below the seafloor in the Nile fan, the eastern flank of which extends into the Levant Basin (Ben-Zeev and Gvirtzman, 2020; Sagy et al., 2020; Tayber et al., 2019). The
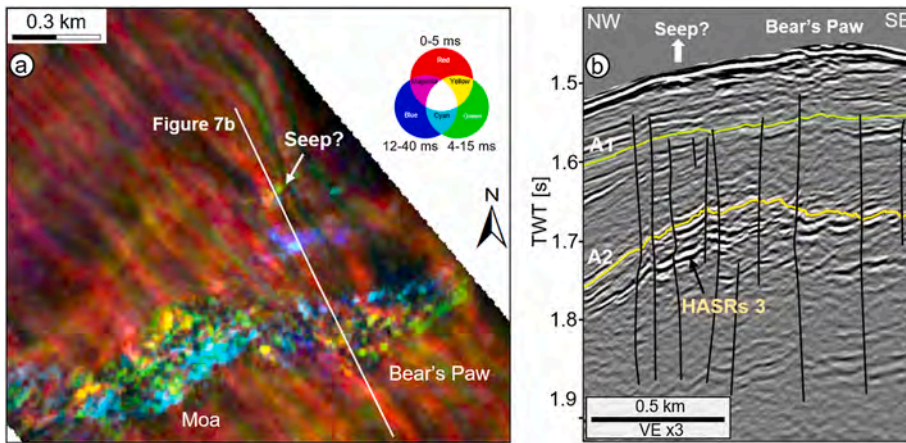
Fig. 7. (a) A zoomed part of the multilevel RGB composite of Fig. 6d, covering the vicinity of Bear's Paw and Moa seeps. (b) A NW-SE seismic profile from the Omakere 3D seismic dataset across the Bear's Paw seep site and reflectivity anomaly to the NW of it (see (a) for the profile outline (white)), showing that the Bear's Paw seep site and nearby anomalous reflectivity site are characterized by seafloor depressions with underlying faults that deform the high amplitude reflections of HASRs 3. TWT[s]: Two-Way Time in Seconds.
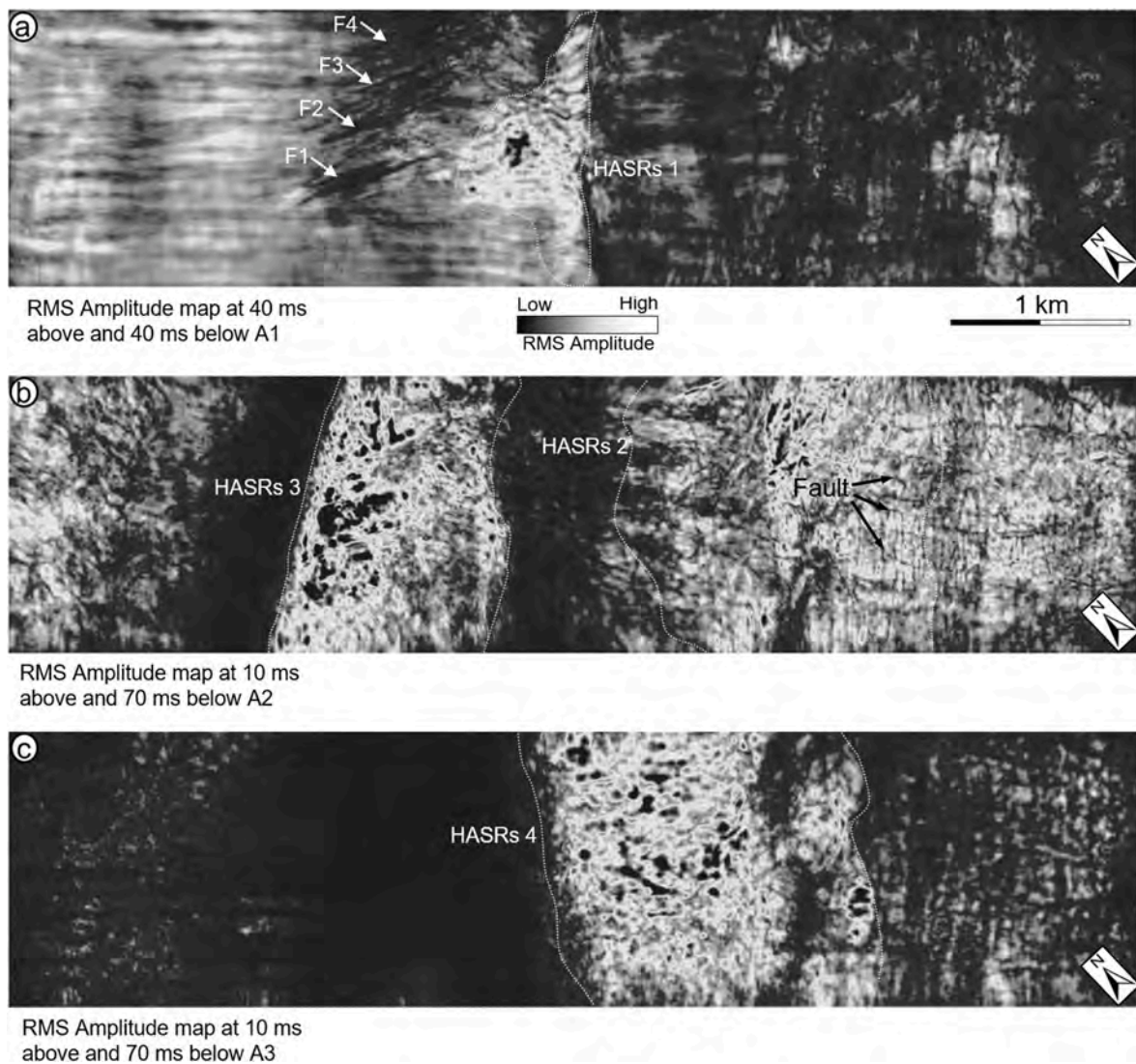

Fig. 8. (a) RMS amplitude map, extracted from 40 ms above to 40 ms below the A1 horizon in the Omakere 3D seismic dataset, highlighting the location and distribution of the anomalous reflections characterizing HASRs 1. Dark sub-parallel lines observed to the north of HASRs 1 represent faults: F1–F4. (b) A RMS amplitude map, extracted from 10 ms above to 70 ms below the A2 horizon, highlighting the distribution of anomalous reflections characterizing HASRs 3 and HASRs 2. Dark stripes highlight multiple faults that offset HASRs 2. (c) An RMS amplitude map, extracted from 10 ms above to 70 ms below horizon A3, highlighting the ~1 km wide N–S oriented HASRs 4.
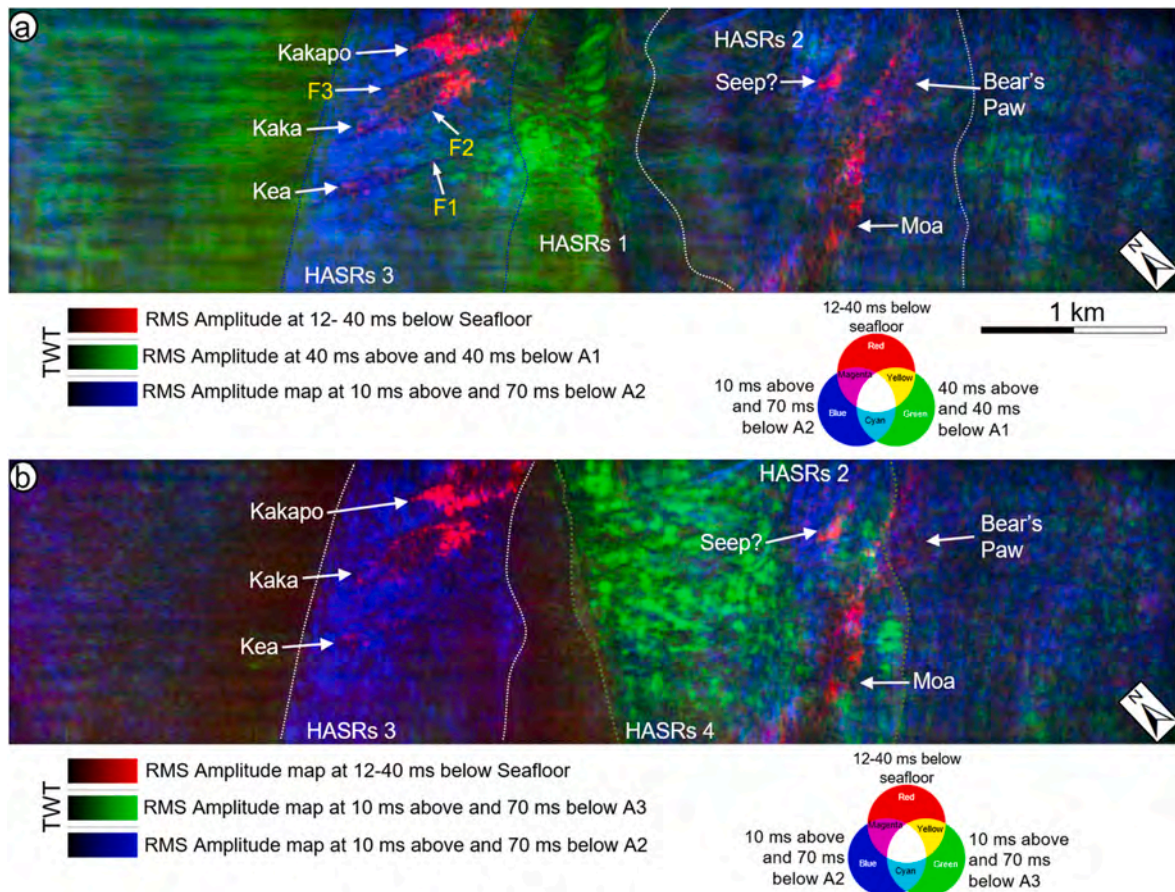
Fig. 9. **(a)** A multilevel RGB composite of the amplitude maps in Fig. 6c (12–40 ms below the seafloor, red), Fig. 8a (40 ms above to 40 ms below horizon A1, green) and Fig. 8b (10 ms above to 70 ms below horizon A2, blue). **(b)** A multilevel RGB composite of the amplitude maps in Fig. 6c (12–40 ms below the seafloor, red), Fig. 8a (40 ms above to 40 ms below horizon A1, green), and Fig. 8c (10 ms above to 70 ms below horizon A2, blue). For better imaging results the green represents here the deepest level, in difference with the other multilevel RGB composites presented in this paper. Note the enhanced illumination of the top, red, level of the multilevel amplitude responses below the seafloor seeps, as highlighted in cyan in Fig. 6d. This reflectivity identified below the Kea, Kaka and Kakapo seeps appears to be spatially related with faults F1–F4 and the overlap of the edges of HASRs 1 and HASRs 3. The Moa and Bear's Paw seeps, as well as the anomaly to the north of the latter, are spatially associated with the overlap of the edges of HASRs 2 and HASRs 4. (For interpretation of the references to color in this figure legend, the reader is referred to the Web version of this article.)

sediments occur within multiple intervals (Tayber et al., 2019), are deposited within a northeast-southwest (NE-SW)-oriented depocenter in the deep basin, and pinch out on the present-day continental shelf (Sagy et al., 2020). Downslope sediment flows and landslides, such as those in the eastern Levant margin (Eruteya et al., 2016; Frey-Martinez et al., 2005; Gadol et al., 2019; Katz et al., 2015) are secondary sources of sediments, complementing Nile-derived sediment supply to the deep basin. Increasing load of the Nile cone Plio-Quaternary sediments produced a northward push and triggered mobilization and deformation of the Messinian salts and overlaying sediments across the eastern Mediterranean since the Pliocene (Ben-Zeev and Gvirtzman, 2020; Bertoni and Cartwright, 2006; Cartwright et al., 2012; Gvirtzman et al., 2017; Zucker et al., 2020). In the Levant Basin, this deformation is recorded in the form of several fold ridges and faults, many of which are observed on the present-day seafloor, where they interact with deep-sea channels (Clark and Cartwright, 2009; Gvirtzman et al., 2015; Zucker et al., 2017).

4.1.2. Multilevel Composition of buried deep sea channel systems

The bathymetry of the study area comprises (a) NNW-SSE trending ridges that are prominent in the western and eastern parts of the study area and are deformed by lineaments with varying orientations (Fig. 3a). The ridges are suggested to belong to the larger circum-Nile deformation belt (Gvirtzman et al., 2015), which formed following shortening that

resulted from the out-squeezing of salts from the Nile delta towards the NNE (Cartwright and Jackson, 2008; Netzeband et al., 2006). (b) A NNW-SSE oriented deep-water channel system, with a prominent sinuous seafloor channel, the Levant channel (Gvirtzman et al., 2015), extending across the center of the study area from south to north. This channel is ~34 km long within the study area, 300–500 m wide and ~30 m deep with respect to the surrounding. The marks of several additional, apparently abandoned and partly buried, channel elements are apparent around and to the west of it (Fig. 3a).

Following Multilevel Composition (Fig. 3b), a multitude of older channels, lobes and crevasse splays are revealed to make up the sedimentary fill, around the prominent ridges (dark) in the western and central parts of the study area. These features are characterized by red, green, and blue colors and their derivatives, which denote shallow (15–30 m, red) to deep (55–120 m, blue) occurrence of the paleo-depositional features within the dataset, respectively. Conversely, a shut-off of composed amplitude, marking the absence of channels systems, characterize the easternmost part of the study area, near the base of the southeastern continental margin of the Levant (Fig. 3b). The full abundance of paleo-depositional features is also observed on a spectral decomposition image of the same interval (Fig. 3c). However, in this case color coding represents the frequency content of the seismic signal, which is associated with different thicknesses of the depositional features imaged and not their stacking pattern. A comparison of Fig. 3b and

c demonstrates the complementary utility of the commonly used spectral decomposition and our new Multilevel Composition maps.

A seismic profile across the study area reveals that the paleo-depositional features mapped by the Multilevel Composition are imaged as pervasive, multilevel and discontinuous high-amplitude bands of reflections (Fig. 3d). These reflections pinch-out at ridge flanks in the eastern part, where they are replaced by more continuous, smooth and dominantly low-amplitude reflections (Fig. 3d). The low-amplitude reflections manifest the shut-off of composed amplitudes in the eastern part (Fig. 3b). Several previous studies have suggested that sediment supply to the deep basin in the Quaternary is mainly by Nile-derived deep-water channels and lobes (Folkman and Mart, 2008; Kanari et al., 2020; Niyazi et al., 2018; Sagy et al., 2020; Tayber et al., 2019). Sediment supply in the basin margin is by alongshore transport, followed by sediment descent along the continental slope and rise (Schattner and Lazar, 2016). Consequently, it is suggested that the marked variation in the composed amplitude response between the two areas i.e. occurrence of channels and crevasse splays across multiple depths in the west and their absence in the eastern part, evidences the primary differences in sedimentation patterns in the area in the later part of the Quaternary.

Multilevel Composition (Fig. 4a) delineates the paleo-Levant Channel, paleo-channels A-D, and several smaller paleo-channels. Evidence for the occurrence of the paleo-Levant Channel is that an older channel, similar to the present-day Levant Channel, is observed at its location (Fig. 3a–b and 4). On seismic reflection profiles, the paleo-channels are characterized by U- or V-shaped depressions and low- to high-amplitude infills (Fig. 4b–c). The low- to high-amplitude infills could indicate lithology changes, for instance, sand- and mud-bearing lithologies, respectively (Posamentier, 2003). The paleo-Levant Channel is associated with a dominant green color on the multilevel composed amplitude map, which indicates that it extends stratigraphically between 25 and 60 m below the seafloor, the intermediate stratigraphic level within the interval of interest. Complementing this detail are minor color variations, which seem to correspond to changes in the internal character of the channel on the spectral decomposition image (Fig. 3c and Supplementary Fig. 1). On the seismic reflection data, the present-day Levant Channel is characterized by low amplitude reflections that reduce in thickness on its two sides (Fig. 4b), likely indicating mud-prone levees (Posamentier, 2003).

The paleo-Levant Channel and paleo-channels A and D display evidence of intense avulsion, indicated by multiple meander scrolls below the channels on the multilevel composed amplitude map and bent reflections on seismic data (Fig. 4a, b, d, and e). These indicate lateral migration and vertical aggradation (Kolla et al., 2007; Posamentier and Kolla, 2003). The paleo-Levant Channel and paleo-channels A and D have high sinuosity, while paleo-channels B and C have low sinuosity. Increase in sinuosity is observed in the northern part of paleo-channel C (Fig. 3b–c and 4a and d). Since the paleo-seafloor was mainly shaped by salt-deformation-related ridges, the substantially similar sinuosity of most of the paleo-channels may be partly due to their response to slope gradient and confinement changes (Clark et al., 1992; Peakall et al., 2012). This may also be due to an overall low energy and muddy flow into the study area from the Nile cone, as sinuous channels are generally linked to low energy muddier flow (Janocko et al., 2013).

Multilevel Composition shows remarkable interaction between paleo-channels as the paleo-Levant Channel (green) is seen to merge with or cross the path of the older (blue) paleo-channel A in its northern portion (yellow arrows in Fig. 4a and d). As the channels cross, the paleo-Levant Channel (green) assumes the flow path of paleo-channel A and incises into its underlying fill (blue). Paleo-channel A fills are identified as high-amplitude seismic reflections below the Levant Channel on seismic reflection data (Fig. 4c). Paleo-channels C and D are observed to merge in the northern section of the study area (Fig. 4a). Consequently, Multilevel Composition adequately highlights the strong interaction between these multi-depth paleo-channels. The merger of

these channels is also visible on the spectral decomposition image, which highlights the differences in the internal character of these features rather than their relative position and stacking pattern (Fig. 3c). Kanari et al. (2020) have suggested that the Levant Channel alone crosses the path of about ten different older channels, indicating that channel merging or crossing relationship is not limited to the study area but a regional feature.

Furthermore, Multilevel Composition (Fig. 4a and d) reveals several dendritic and small channels up north of paleo-channel B and between the paleo-Levant Channel and paleo-channel A. The later set of small channels are directed north-eastward, where they extend northwards towards sedimentary deposits that spill-out from a bend along the Levant Channel. Similar spill-out or off-flank deposits are also identified in the northern section of the Levant Channel, where they are associated with several north-oriented dendritic channels. These deposits are predominantly characterized by a mixture of red and yellow colors on the composed amplitude map (Fig. 4a and d). The yellow color is an intermix of red (15–30 m below the seafloor) and green (25–60 m below the seafloor) colors, representing the presence of these features about 25–30 m below the seafloor. The features characterized by red are the shallowest, and possibly youngest stratigraphic features, or are possibly associated with lower overburden accumulation rates.

In addition, the spill-out deposits are characterized by continuous to jagged or serrated high amplitude reflections with associated V-shaped depressions on seismic reflection profiles (Fig. 4b). Based on their appearance on the multilevel composed amplitude map and seismic profile, the deposits are interpreted as crevasse splays (Burns et al., 2017; Gulliford et al., 2014), while the jagged reflections represent small channels within them – a distributary channel network. The crevasse splay deposits may be related to the spill-out and deposition of sediments over the bank of the Levant Channel. This could happen as flow breached the less competent levee, acting as the confining wall of the channel, during periods of enhanced flow from the Nile system into the study area. In general, the occurrence of channels and crevasse splays within the study area may reflect a period of elevated sediment supply. This is possibly in response to enhanced Nile-derived sediment flux into the Levant Basin in parts of the Quaternary (Ben-Gai et al., 2005; Sagy et al., 2020).

In terms of ridge-flow interactions, Multilevel Composition reveals that the paleo-depositional features generally deviate away from the ridges (Figs. 3b and 4a). The features are observed as reflections pinching out towards ridge flanks on seismic reflection data (Fig. 4c). This may be caused by the increase in paleo-elevation as the depositional elements approach the ridges, which were already areas of positive seafloor topography. It is observed from the multilevel composed amplitude map (Fig. 4a) and on a seismic profile (Fig. 4c) that the occurrence of the ridges caused facies to migrate towards topographic lows. Consequently, observations from Multilevel Composition reveal that inherited topography dictates the localization of flow and sedimentation in topographic lows in the study area. Flow diversion by ridges, as shown via Multilevel Composition, in the study area seems to be occurring over a large part of the Levant Basin. Similar relationships have been shown from deeper parts of Nile fan in the Levant Basin (Clark and Cartwright, 2009; Zucker et al., 2017), as well as other geological settings, such as the Niger Delta (Jolly et al., 2016).

Overall, our analysis, using the multilevel composed amplitude map of the study interval, reveals that the study area is characterized by paleo-depositional features, most of which occur across multiple intervals. This could indicate that the features belong to different evolutionary phases. Consequently, Multilevel Composition (Figs. 3b and 4a and d) is able to reveal meaningful color-coded depth information, which provide novel additions towards understanding the evolution of the depositional features. Hence, the new method provides an easier to understand and easier to interpret view of the channels in terms of their evolution than spectral decomposition. In general, Multilevel Composition reveals that Nile-derived sediments are deposited in the study area

by two dominant flow types; (a) confined flow via predominant high sinuosity channel systems and (b) unconfined flow via crevasse splays.

4.2. Omakere Ridge, Hikurangi Margin, New Zealand

The second case study area is the Omakere Ridge on the Hikurangi Margin, New Zealand (Fig. 1b). Verified seep sites, including Kea, Kaka, Kakapo, Moa and Bear's Paw (Fig. 5) and their faunal assemblages constitute extensive evidence of active microbial methane discharge at the ridge. Additional evidence of seepage include several authigenic carbonate slabs at the seeps and gas hydrate recovered below the Bear's Paw site (Barnes et al., 2010; Faure et al., 2010; Greinert et al., 2010; Jones et al., 2010). Migrating fluids within the Omakere Ridge are generally channeled from deep, biogenic sources into the hydrate zone before eventually escaping at seafloor sites (Plaza-Faverola et al., 2014; Watson et al., 2020). The seep sites are linked to deeper gas-bearing intervals through several complex fault systems (Plaza-Faverola et al., 2014). However, the relationship between the seeps, faults and deeper gas-bearing intervals as well as the extents of the seeps are not well known.

The goals of utilizing Multilevel Composition here were: to illuminate the seeps, determine their full extent, and better constrain their links to underlying potential gas-bearing intervals. In the evaluation of the Omakere 3D seismic dataset, it was determined that the anomalous seismic responses connected to the seafloor (0 ms) seeps are within up to 40 ms below the seafloor. An investigation of the vertical distribution of these features revealed that it would be useful to use the seafloor as the reference horizon and consider the intervals 0–5 ms, 4–15 ms and 12–40 ms below it. The maximum positive amplitudes for the three windows were extracted and were subsequently blended in RGB color space (Fig. 6). To reveal the connection between the seafloor seeps and sub-surface gas-bearing intervals, three reference horizons: A1, A2 and A3 were identified, following Plaza-Faverola et al. (2014), and mapped across the dataset. The RMS amplitude maps of these horizons were computed and selectively co-rendered with selected maximum amplitude maps from the three shallow sub-windows (Figs. 6, 8 and 9).

4.2.1. Regional geology

The Hikurangi margin, an extensive gas hydrate province (Pecher et al., 2010), is a component of the active Kermadec-Hikurangi subduction zone situated at the boundary where the Pacific Plate subducts obliquely beneath the Australian Plate (Fig. 1b; Beavan et al., 2002). The Omakere Ridge is located on the central part of the Hikurangi margin, a region that is dominated by accretion (Jones et al., 2010) and characterized by NE-SW oriented slope parallel anticlinal ridges. One of these is the Omakere Ridge with a relief of ~500 m at water depths of 1100–1200 m (Barnes et al., 2010). Underlying the easternmost flank of the ridge are an active thrust and a deeper inactive thrust imbricate (Barnes et al., 2010). These structures are complemented by another active thrust splay that reaches the seafloor around the center of the ridge i.e. the "central thrust" (Plaza-Faverola et al., 2014). The ridge is underlain by a wedge of Cretaceous and Paleogene rocks. These underlie folded Miocene to Recent sediments in the hanging wall of the lower thrust faults. Several active seeps, including the Kea, Kaka and Kakapo (Faure et al., 2010; Greinert et al., 2010; Jones et al., 2010) lie in the hanging wall of the central thrust, while the Bear's Paw and Moa seeps lie in the footwall of the thrust.

4.2.2. Observations from seismic reflection data

The seafloor seeps in the study area are associated with five elongated seafloor depressions, which represent the Kea, Kaka, Kakapo, Moa and Bear's Paw cold seeps (Fig. 5a). The Kakapo, Kaka, and Kea seeps are individually oriented NNW-SSE and collectively E-W-oriented, while the Bear's Paw and Moa seeps are ENE-WSW oriented. Seeps within the Omakere Ridge are associated with underlying anomalous high amplitude seismic reflections (HASRs) or bright spots (Fig. 5b–d). The

anomalies are linked to underlying zones of vertically blanked reflections on seismic reflection profiles. A set of faults: F1–F4 are observed below the Kea, Kaka and Kakapo seeps (Fig. 5c), extending between deeper HASRs (1–4) to shallower intervals below the seafloor seeps. The shallowest, HASRs 1 is identified in proximity of horizon A1, within 0.1 s of the seafloor (Fig. 5b). Seismic reflections representing HASRs 2 are faulted and located at about 0.2 s beneath the Moa and Bear's Paw seep sites (Fig. 5b). Similarly, HASRs 3 is faulted and observed below the Kaka, Kea and Kakapo seep sites. HASRs 3 appears to be connected to shallower intervals below the seeps by faults F1–F4. HASRs 4 is folded and faulted and represents the deepest of the HASRs analyzed in the study area (Fig. 5b). HASRs 1–4 are suggested by Plaza-Faverola et al. (2014) to manifest fluid-bearing sediments. In addition, localized sub-seep HASRs or bright spots are identified on the amplitude maps extracted from 0 to 5 ms, 4–15 ms and 12–40 ms below the seafloor (Fig. 6a–c). An additional near-seafloor localized high amplitude anomaly is observed ~0.1 km west of the Bear's Paw seep site though its link to known seeps is not clear.

4.2.3. Multilevel Composition of the seafloor seeps and deeper gas-bearing intervals

Multilevel Composition of amplitude maps computed at sub-windows below the seafloor adequately illuminates the five seep sites as localized high amplitude zones with varying colors and intensities (Fig. 6d). While the composed amplitude at the Kea, Kaka and Kakapo seep sites are mutually distinguishable, the composed amplitude at the Bear's Paw and Moa sites appear continuous, revealing a significant interlink between the two seep sites. Clearly delineated by the Multilevel Composition method, this linkage was first suggested by Jones et al. (2010) based on sidescan sonar imaging. Additionally, Multilevel Composition reveals a larger extent and intensity of deeper reflectivity (at ~20 ms; cyan) beneath the northern part of Moa, and shallower and lower intensity reflectivity beneath the southern part of Moa and Bear's Paw. Together the mutual interlink and relative depths may suggest lateral flow of gas in the shallow subsurface from the northern part of Moa southwards and northwards. The areas of the seeps are estimated based on their multilevel composed amplitude responses (Fig. 6d) as ~0.11 km^2 for Kea, ~0.17 km^2 for Kaka, ~0.18 km^2 for Kakapo and ~0.5 km^2 for Moa and Bear's Paw. The main part of the Bear's Paw site has an area of ~0.18 km^2 (Fig. 6d).

In addition, at ~0.1 km to the west of the Bear's Paw is an additional multilevel composed amplitude anomaly with an area of ~0.07 km^2 (Figs. 6d and 7a). Seismic reflection data (Fig. 7b) reveal that it is associated with a seafloor depression and underlying localized HASRs, which are linked to similar HASRs below the Bear's Paw. It is also underlain by faults that reach HASRs 3 at depth, extend upwards and terminate in shallow sediments below the seafloor anomaly (Fig. 7b). These observations suggest the feature is either an extension of the Bear's Paw seep or another distinct seep site that had not been discovered previously. The absence of any significant linkage between this suspected seep and the Bear's Paw, at least in their multilevel composed amplitude responses, supports the later interpretation.

Colored highlights in the multilevel RGB composed amplitude image (Fig. 6d) represent the depth of elements that are presumably associated with the gas seepage system, based on the sub-windows used. For instance, the green color in the western end of the Kaka seep (Fig. 6d) indicate the predominance of bright seismic reflections, representing probably seep-related features, within 4–15 ms below the seafloor. The bright cyan color at the eastern end of this seep (Fig. 6d) indicates the deeper presence of intensely reflective features at the overlap of the 4–15 ms and 12–40 ms intervals below the seafloor. Together these may represent a lateral westward migration of gas in the sub-surface. The brightest reflections imaged in association with the seeps are cyan, suggesting that the primary gas accumulations are imaged ~15 ms below the surface. The overall intensity differs between the different seeps.

Of the five verified seep sites in the study area, the dimmest composed amplitude response is associated with the Bear's Paw site, followed by the Kea seep site (Fig. 6d). The brightest composed amplitude responses are associated with Kakapo (highest), Kaka, and the northern part of Moa (lowest). These responses are likely to be associated with seafloor and sub-seafloor features at the seep sites. This result contrasts previously published ranking based on surface observations. Bear's Paw and Kea sites were found to have the highest population densities of living chemosynthetic organisms, while having the least significant carbonate structures (Greinert et al., 2010; Jones et al., 2010). Moreover, Bear's Paw was found to have the highest methane concentrations in the water column, recorded up to several hundreds of meters above the seeps (Faure et al., 2010). On the other hand, the Kakapo, Kaka, and Moa seeps host the most significant carbonate structures and shells, as well as a variety of living seep-related biota, indicating long lasting to present-day activity (Jones et al., 2010). Based on these seafloor observations and results of sidescan sonar imaging, Jones et al. (2010) ranked the Bear's Paw seep as the most active seep, followed by Kea, the southwestern end of Moa, Kaka, Kakapo, and the northeastern end of Moa seeps (Fig. 6d). Thus, the most active seeps with less carbonates match areas with dim composed amplitude responses, while the least active seeps with more carbonates match areas with bright composed amplitude responses (Fig. 6d).

It is possible that the Multilevel Composition responses reflect the presence of seafloor authigenic carbonates and hardgrounds, which are generally characterized by high amplitude anomalies on seismic reflection data (Roberts et al., 2006). Alternatively, this discrepancy may be associated with the relatively large depth (~15 ms) of the brightest reflections, suggesting that the presently less active sites may be associated with deep accumulations of gas, while active sites are associated with smaller shallower gas accumulations. Taken together, these observations could suggest that past precipitation of pervasive authigenic carbonates sealed the now less active seepage site, while alternative interpretations may exist. Notably, the application of the Multilevel Composition method highlighted this previously underappreciated discrepancy between the results of seismic imaging and seafloor observations.

Another significant result obtained by Multilevel Composition in this area is the revelation that the Moa, Kakapo, and Kaka sites are each characterized by two distinct zones (Fig. 6d). The Kakapo site consists of an eastern region with bright multilevel composed amplitude and a western region with dimmed multilevel composed amplitude. The Kaka site consists of an eastern end with dimmed composed amplitude and a western end with bright composed amplitude (Fig. 6d). The Moa site is composed of a main northeastern region with bright composed amplitude and a southwestern region with dimmed composed amplitude (Figs. 6d and 7a). These results of Multilevel Composition at the Moa site favorably match seafloor observations of Jones et al. (2010). They show that the site is composed of a northeastern end with very high relief carbonate rocks, corals and non-seep fauna, and a southwestern end that supports chemosynthetic fauna. Consequently, our analysis indicates that the bright cyan (northwestern end) and dimmed (southwestern end) signals at the Moa site reflect the abundance of carbonate rocks at the northwestern end and their paucity at the southwestern ends, respectively. Based on these observations, it is suggested that like the Moa, the Kakapo and Kaka sites are perhaps made up of two zones with varying abundance of seep-related features and hence varying degree of activity.

To investigate the connection of deeper reflections with the seafloor seeps a set of RMS amplitude maps were extracted with the reference horizons being A1, A2 and A3 (Fig. 8). We find that HASRs 1 is located to the southeast of four near-parallel NW-SE oriented faults (F1–F4) and extends over an area of up to ~0.89 km^2 (Fig. 8a). HASRs 2 and HASRs 3 extend over areas of 2.34 km^2 and 1.68 km^2 respectively in the vicinity of horizon A2, while HASRs 4 extends over an area of ~2.89 km^2 around horizon A3 (Fig. 8b–c). Multilevel composition of these amplitude maps (Fig. 9) help to constrain the relative positions of the deeper elements

with respect to the seep areas (highlighted in red). The Kea, Kaka and Kakapo seeps and their underlying near-parallel faults are directly spatially positioned above HASRs 3 (see the bright red color representing the seeps in Fig. 9a). HASRs 1 overlaps with the southeastern edge of HASRs 3, with its edge underlying the northeastern seeps. However, it does not show any connection to HASRS 2 (Fig. 9a). The edges of both HASRs 4 and HASRS 2 are overlapped beneath the Bear's Paw and Moa seeps (Figs. 5b and 9b). Based on these observations, we infer that gas escaping from the Kea, Kaka and Kakapo seeps may be derived from the combination of fluids migrating from HASRs 3 and HASRs 1. Gases escaping at the Bear's Paw and Moa sites may be derived from the combination of fluids migrating from HASRs 4 and HASRs 2. Taken together the Multilevel Composition of amplitude maps (Fig. 9) suggest that fluids are routed sub-vertically upward from deeper elements to the seeps. Beneath the Kea, Kaka, and Kakapo seeps this migration may be routed along faults F1–F4, as suggested by the alignment and spacing of the three seeps mimicking the style of the underlying faults F1–F4 (Fig. 5b–c and 9). Faults identified below the Moa and Bear's Paw seeps (Fig. 5b and d, 8b and 9a) are suspected migration pathways for sub-vertical upward migration of fluids to shallower intervals below the Bear's Paw and Moa seeps.

5. Discussion

The case studies presented here provide a basic demonstration of the utility of Multilevel Composition for robust visualization of complex geological features over a relative depth range in a single intuitive map. The method allows an interpreter to effectively visualize and characterize geological features and, importantly, to decode in colors normally hidden depth information. This is done with minimal effort, as only the reference horizon needs to be picked in a rigorous manner. The composed maps allow to derive high level morphological understandings, which delineate the controlling processes, and can also be utilized to aid in more detailed mapping of complex reflectivity patterns.

We demonstrate the efficacy of the method by combining multi-level amplitude maps in two different geological settings and types of datasets and investigating two different processes. In the eastern Nile deep-sea fan, standard commercial hydrocarbon exploration seismic data was interpreted to characterize classical deep-water depositional elements with respect to the seafloor surface. The method revealed depth-related information, which was used to infer details about the evolution of the depositional elements. We demonstrate the complementary utility of our new Multilevel Composition method with the commonly used and similarly looking spectral decomposition. Spectral decomposition provides detailed structural information, associated with changes in thickness of the depositional features, while Multilevel Composition constrains the relative positions of the different elements. On the Hikurangi Subduction Margin, seafloor cold seep sites and their underlying gas migration systems were characterized from 3D high-resolution P-Cable data. Here a combination of several different multilevel composition maps was used. In each example, the method promoted the visual integration of three multilevel attribute maps at the same time. Multilevel Composition greatly increased the value of the seismic attributes and enhanced visualization power. In the eastern Nile fan, it deciphered the interdependence of multiple generations of the deep-sea channels system visualized, while highlighting a range of related depositional features. At the Omakere ridge, it was not only useful at detecting and characterizing seafloor seeps, but also at providing novel insights into their activity.

Multilevel Composition provides a simple, straight-forward five-step approach that works well in stratigraphically complex settings with lateral facies variations and difficult-to-pick seismic horizons, similar to the Quaternary of the eastern Nile fan. It also works well in less complex settings where there is an interest in co-evaluation of multiple intervals, such as in the Omakere Ridge. In both study areas, we focused on amplitude-derived attributes. However, Multilevel Composition will

work adequately where geological features such as sand-bearing channels and lobes, mass transport deposits, volcanics, carbonate-hosting seeps, hydrocarbon-bearing intervals, faults and more stand out from the background data. In addition, Multilevel Composition may be used for blending other attributes, e.g., coherence, instantaneous phase, energy and frequency-based attributes, and can utilize other color models, further expanding its potential applicability. Multilevel Composition therefore has a broad scope of potential applications in basin analysis, subsurface resource, storage and sequestration assessment and characterization, offshore seep and minerals investigation, seafloor habitats mapping, geohazard assessment for onshore and offshore sites and marine planning at large.

6. Conclusions

We here propose an innovative method for 3D seismic interpretation, involving color blending of multilevel attribute maps. The method produces a single image map, in which inter-window/layer depth reflectivity information is coded in colors. This map characterizes the relative spatiotemporal distribution of intricate multi-depth geological features with respect to reference horizons. Here we demonstrate the efficacy of Multilevel Composition to characterize (a) buried channels and crevasse splay systems in the eastern Nile fan in the Levant Basin, eastern Mediterranean; and (b) cold seeps and their links to deeper gas-bearing intervals on the Omakere Ridge along the Hikurangi Margin, offshore New Zealand. We anticipate Multilevel Composition to become straight-forward to include in other interpretation workflows and will find wide application for studies linking several sub-surface depth levels, such as subsurface resource and storage characterization, fluid-flow related investigations, basin analysis, characterization of seafloor habitats and geohazard assessment.

Declaration of competing interest

The authors declare that they have no known competing financial interests or personal relationships that could have appeared to influence the work reported in this paper.

Data availability

Data availability is noted in the manuscript data availability section

Acknowledgments

Appendix A. Supplementary data

Supplementary data to this article can be found online at https://doi.org/10.1016/j.marpetgeo.2022.105938.

References

Al-Shuhail, A.A., Al-Dossary, S.A., Mousa, W.A., 2017. Color display of seismic images. In: Seismic Data Interpretation Using Digital Image Processing. https://doi.org/10.1002/9781119125594.ch6.

Alves, T.M., Omosanya, K., Gowling, P., 2015. Volume rendering of enigmatic high-amplitude anomalies in southeast Brazil: a workflow to distinguish lithologic features from fluid accumulations. Interpretation 3. https://doi.org/10.1190/INT-2014-0106.1.

Bacon, M., Simm, R., Redshaw, T., 2010. 3-D Seismic Interpretation. Cambridge University Press. https://doi.org/10.1017/CBO9780511802416.

Barnes, P.M., Lamarche, G., Bialas, J., Henrys, S., Pecher, I., Netzeband, G.L., Greinert, J., Mountjoy, J.J., Pedley, K., Crutchley, G., 2010. Tectonic and geological framework for gas hydrates and cold seeps on the Hikurangi subduction margin, New Zealand. Mar. Geol. 272 https://doi.org/10.1016/j.margeo.2009.03.012.

Beavan, J., Tregoning, P., Bevis, M., Kato, T., Meertens, C., 2002. Motion and rigidity of the Pacific Plate and implications for plate boundary deformation. J. Geophys. Res. Solid Earth 107. https://doi.org/10.1029/2001jb000282.

Ben-Gai, Y., Ben-Avraham, Z., Buchbinder, B., Kendall, C.G.S.C., 2005. Post-Messinian evolution of the Southeastern Levant Basin based on two-dimensional stratigraphic simulation. Mar. Geol. https://doi.org/10.1016/j.margeo.2005.03.003.

Ben-Zeev, Y., Gvirtzman, Z., 2020. When two salt tectonics systems meet: gliding downslope the levant margin and salt out-squeezing from under the nile delta. Tectonics 39. https://doi.org/10.1029/2019TC005715.

Bertoni, C., Cartwright, J.A., 2006. Controls on the basinwide architecture of late Miocene (Messinian) evaporites on the levant margin (eastern Mediterranean). Sediment. Geol. https://doi.org/10.1016/j.sedgeo.2006.03.019. .

Brown, A.R., 2001. Understanding seismic attributes. Geophysics. https://doi.org/10.1190/1.1444919.

Brown, A.R., 1991. Interpretation of Three-Dimensional Seismic Data. https://doi.org/10.1190/1.9781560802884 third ed.. Interpret. three-dimensional Seism. data. third ed.

Burns, C.E., Mountney, N.P., Hodgson, D.M., Colombera, L., 2017. Anatomy and Dimensions of Fluvial Crevasse-Splay Deposits: Examples from the Cretaceous Castlegate Sandstone and Neslen Formation, vol. 351. U.S.A. Sediment. Geol, Utah. https://doi.org/10.1016/j.sedgeo.2017.02.003.

Cao, J., Yue, Y., Zhang, K., Yang, J., Zhang, X., 2015. Subsurface channel detection using color blending of seismic attribute volumes. Int. J. Signal Process. Image Process. Pattern Recognit. 8 https://doi.org/10.14257/ijsip.2015.8.12.16.

Cao, J., Zhang, X., Wang, Y., Zhao, Q., 2016. Subsurface geobody imaging using CMY color blending with seismic attributes. J. Electr. Comput. Eng. https://doi.org/10.1155/2016/9181254, 2016.

Cartwright, J., Jackson, M., Dooley, T., Higgins, S., 2012. Strain partitioning in gravity-driven shortening of a thick, multilayered evaporite sequence. Geol. Soc. Spec. Publ. https://doi.org/10.1144/SP363.21.

Cartwright, J.A., Jackson, M.P.A., 2008. Initiation of gravitational collapse of an evaporite basin margin: the Messinian saline giant, Levant Basin, eastern Mediterranean. Bull. Geol. Soc. Am. https://doi.org/10.1130/B26081X.1.

Chaves, M.U., Di Marco, L., Kawakami, G., Oliver, F., 2011. Visualization of geological features using seismic volume rendering, RGB blending and geobody extraction. In: Proceedings of the 12th International Congress of the Brazilian Geophysical Society & EXPOGEF. Rio de Janeiro, Brazil, pp. 848–850. https://doi.org/10.1190/sbgf2011-175.

Chopra, S., Marfurt, K., 2006. Seismic Attributes – A Promising Aid for Geologic Prediction. CSEG Rec, 2006 Spec.

Chopra, S., Marfurt, K.J., 2007. Seismic Attributes for Prospect Identification and Reservoir Characterization, Seismic Attributes for Prospect Identification and Reservoir Characterization. https://doi.org/10.1190/1.9781560801900.

Chopra, S., Marfurt, K.J., 2005. Seismic attributes - a historical perspective. Geophysics. https://doi.org/10.1190/1.2098670.

Clark, I.R., Cartwright, J.A., 2009. Interactions between submarine channel systems and deformation in deepwater fold belts: examples from the Levant Basin, Eastern Mediterranean sea. Mar. Petrol. Geol. https://doi.org/10.1016/j.marpetgeo.2009.05.004.

Clark, J.D., Kenyon, N.H., Pickering, K.T., 1992. Quantitative analysis of the geometry of submarine channels: implications for the classification of submarine fans. Geology 20. https://doi.org/10.1130/0091-7613(1992)020<0633:QAOTGO>2.3.CO.

Eruteya, O.E., Safadi, M., Waldmann, N., Makovsky, Y., Ben-Avraham, Z., 2016. Seismic geomorphology of the Israel slump complex in the Levant Basin (SE Mediterranean). In: Advances in Natural and Technological Hazards Research. https://doi.org/10.1007/978-3-319-20979-1_4.

European Marine Observation and Data Network (EMODNET), 2020. Bathymetry of the European Seas. 2. Feb. 2022. Downloaded from. https://portal.emodnet-bathymetry.eu/.

Faure, K., Greinert, J., von Deimling, J.S., McGinnis, D.F., Kipfer, R., Linke, P., 2010. Methane seepage along the Hikurangi Margin of New Zealand: geochemical and physical data from the water column, sea surface and atmosphere. Mar. Geol. 272 https://doi.org/10.1016/j.margeo.2010.01.001.

Folkman, Y., Mart, Y., 2008. Newly recognized eastern extension of the Nile deep-sea fan. Geology. https://doi.org/10.1130/G24995A.1.

Frey-Martinez, J.F., Cartwright, J., Hall, B., 2005. 3D seismic interpretation of slump complexes: examples from the continental margin of Israel. Basin Res. https://doi.org/10.1111/j.1365-2117.2005.00255.x.

Gadol, O., Tibor, G., ten Brink, U., Hall, J.K., Groves-Gidney, G., Bar-Am, G., Hübscher, C., Makovsky, Y., 2019. Semi-automated bathymetric spectral decomposition delineates the impact of mass wasting on the morphological

evolution of the continental slope, offshore Israel. Basin Res. 12420 https://doi.org/10.1111/bre.12420.

General Bathymetric Chart of the Oceans (GEBCO), 2022. Gridded Bathymetry Data. 2. Feb. 2022. Downloaded from. https://download.gebco.net/.

Greinert, J., Lewis, K.B., Bialas, J., Pecher, I.A., Rowden, A., Bowden, D.A., De Batist, M., Linke, P., 2010. Methane seepage along the Hikurangi Margin, New Zealand: overview of studies in 2006 and 2007 and new evidence from visual, bathymetric and hydroacoustic investigations. Mar. Geol. 272 https://doi.org/10.1016/j.margeo.2010.01.017.

Gulliford, A.R., Flint, S.S., Hodgson, D.M., 2014. Testing applicability of models of distributive fluvial systems or trunk rivers in ephemeral systems: reconstructing 3-D fluvial architecture in the Beaufort Group, South Africa. J. Sediment. Res. 84 https://doi.org/10.2110/jsr.2014.88.

Gvirtzman, Z., Manzi, V., Calvo, R., Gavrieli, I., Gennari, R., Lugli, S., Reghizzi, M., Roveri, M., 2017. Intra-Messinian truncation surface in the Levant Basin explained by subaqueous dissolution. Geology. https://doi.org/10.1130/G39113.1.

Gvirtzman, Z., Reshef, M., Buch-Leviatan, O., Groves-Gidney, G., Karcz, Z., Makovsky, Y., Ben-Avraham, Z., 2015. Bathymetry of the Levant basin: interaction of salt-tectonics and surficial mass movements. Mar. Geol. https://doi.org/10.1016/j.margeo.2014.12.001.

Henderson, J., Purves, S.J., Fisher, G., 2008. Delineation of Geological Elements from RGB Color Blending of Seismic Attribute Volumes, vol. 27. Lead. Edge, Tulsa, OK. https://doi.org/10.1190/1.2896625.

Janocko, M., Nemec, W., Henriksen, S., Warchoł, M., 2013. The diversity of deep-water sinuous channel belts and slope valley-fill complexes. Mar. Petrol. Geol. 41 https://doi.org/10.1016/j.marpetgeo.2012.06.012.

Jolly, B.A., Lonergan, L., Whittaker, A.C., 2016. Growth history of fault-related folds and interaction with seabed channels in the toe-thrust region of the deep-water Niger delta. Mar. Petrol. Geol. 70 https://doi.org/10.1016/j.marpetgeo.2015.11.003.

Jones, A.T., Greinert, J., Bowden, D.A., Klaucke, I., Petersen, C.J., Netzeband, G.L., Weinrebe, W., 2010. Acoustic and visual characterisation of methane-rich seabed seeps at Omakere Ridge on the Hikurangi Margin, New Zealand. Mar. Geol. 272 https://doi.org/10.1016/j.margeo.2009.03.008.

Judd, A., Hovland, M., 2007. Seabed Fluid Flow: the Impact on Geology, Biology, and the Marine Environment, Seabed Fluid Flow: the Impact on Geology, Biology, and the Marine Environment. https://doi.org/10.1017/CBO9780511535918.

Kanari, M., Tibor, G., Hall, J.K., Ketter, T., Lang, G., Schattner, U., 2020. Sediment transport mechanisms revealed by quantitative analyses of seafloor morphology: new evidence from multibeam bathymetry of the Israel exclusive economic zone. Mar. Petrol. Geol. 114 https://doi.org/10.1016/j.marpetgeo.2020.104224.

Katz, O., Reuven, E., Aharonov, E., 2015. Submarine landslides and fault scarps along the eastern Mediterranean Israeli continental-slope. Mar. Geol. 369 https://doi.org/10.1016/j.margeo.2015.08.006.

Kolla, V., Posamentier, H.W., Wood, L.J., 2007. Deep-water and fluvial sinuous channels-Characteristics, similarities and dissimilarities, and modes of formation. Mar. Petrol. Geol. https://doi.org/10.1016/j.marpetgeo.2007.01.007.

Koren, Z., Ravve, I., 2011. Full-azimuth subsurface angle domain wavefield decomposition and imaging Part I: directional and reflection image gathers. Geophysics 76. https://doi.org/10.1190/1.3511352.

Kumar, P.C., Alves, T.M., Sain, K., 2021. Submarine canyon systems focusing sub-surface fluid in the Canterbury Basin, South Island, New Zealand. Sci. Rep. 11 https://doi.org/10.1038/s41598-021-96574-3.

Kumar, P.C., Sain, K., 2020. A machine learning tool for interpretation of Mass Transport Deposits from seismic data. Sci. Rep. 10 https://doi.org/10.1038/s41598-020-71088-6.

Marfurt, K.J., 2015. Techniques and best practices in multiattribute display. Interpretation 3. https://doi.org/10.1190/INT-2014-0133.1.

Netzeband, G.L., Hübscher, C.P., Gajewski, D., 2006. The structural evolution of the Messinian evaporites in the Levantine Basin. Mar. Geol. https://doi.org/10.1016/j.margeo.2006.05.004.

Niyazi, Y., Eruteya, O.E., Omosanya, K.O., Harishidayat, D., Johansen, S.E., Waldmann, N., 2018. Seismic geomorphology of submarine channel-belt complexes in the Pliocene of the Levant Basin, offshore central Israel. Mar. Geol. 403, 123–138. https://doi.org/10.1016/j.margeo.2018.05.007.

Partyka, G., Gridley, J., Lopez, J., 1999. Interpretational Applications of Spectral Decomposition in Reservoir Characterization. https://doi.org/10.1190/1.1438295. Lead. Edge.

Peakall, J., Kane, I.A., Masson, D.G., Keevil, G., Mccaffrey, W., Corney, R., 2012. Global (latitudinal) variation in submarine channel sinuosity. Geology 40. https://doi.org/10.1130/G32295.1.

Pecher, I.A., Henrys, S.A., Wood, W.T., Kukowski, N., Crutchley, G.J., Fohrmann, M., Kilner, J., Senger, K., Gorman, A.R., Coffin, R.B., Greinert, J., Faure, K., 2010. Focussed fluid flow on the Hikurangi Margin, New Zealand — evidence from possible local upwarping of the base of gas hydrate stability. Mar. Geol. 272, 99–113. https://doi.org/10.1016/j.margeo.2009.10.006.

Plaza-Faverola, A., Pecher, I., Crutchley, G., Barnes, P.M., Bünz, S., Golding, T., Klaeschen, D., Papenberg, C., Bialas, J., 2014. Submarine gas seepage in a mixed contractional and shear deformation regime: cases from the Hikurangi oblique-subduction margin. Geochem. Geophys. Geosyst. 15 https://doi.org/10.1002/2013GC005082.

Posamentier, H.W., 2003. Depositional elements associated with a basin floor channel-levee system: case study from the Gulf of Mexico. Mar. Petrol. Geol. 20 https://doi.org/10.1016/j.marpetgeo.2003.01.002.

Posamentier, H.W., Kolla, V., 2003. Seismic geomorphology and stratigraphy of depositional elements in deep-water settings. J. Sediment. Res. https://doi.org/10.1306/111302730367.

Roberts, H.H., Hardage, B.A., Shedd, W.W., Hunt, J., 2006. Seafloor reflectivity - an important seismic property for interpreting fluid/gas expulsion geology and the presence of gas hydrate. Lead. Edge. https://doi.org/10.1190/1.2202667.

Safadi, M., Meilijson, A., Makovsky, Y., 2017. Internal deformation of the southeast Levant margin through continued activity of buried mass transport deposits. Tectonics. https://doi.org/10.1002/2016TC004342.

Sagy, Y., Dror, O., Gardosh, M., Reshef, M., 2020. The origin of the Pliocene to recent succession in the Levant basin and its depositional pattern, new insight on source to sink system. Mar. Petrol. Geol. 120, 104540 https://doi.org/10.1016/j.marpetgeo.2020.104540.

Schattner, U., Lazar, M., 2016. Hierarchy of Source-To-Sink Systems — Example from the Nile Distribution across the Eastern Mediterranean. Sediment. Geol. https://doi.org/10.1016/j.sedgeo.2016.08.006.

Stark, T.J., 2006. Visualization techniques for enhancing stratigraphic inferences from 3D seismic data volumes. https://doi.org/10.1524/icom.2006.5.1.75. First Break 24.

Subrahmanyam, D., Rao, P.H., 2008. Seismic attributes-A review. In: 7th International Conference and Exposition on Petroleum Geophysics.

Tayber, Z., Meilijson, A., Ben-Avraham, Z., Makovsky, Y., 2019. Methane hydrate stability and potential resource in the Levant Basin, southeastern Mediterranean Sea. Geosciences 9, 306. https://doi.org/10.3390/geosciences9070306.

The National Institute for Water and Atmospheric Research (NIWA), 2016. New Zealand Regional Bathymetry. 2 Feb. 2022. Downloaded from. https://niwa.co.nz/our-science/oceans/bathymetry.

Watson, S.J., Mountjoy, J.J., Barnes, P.M., Crutchley, G.J., Lamarche, G., Higgs, B., Hillman, J., Orpin, A.R., Micallef, A., Neil, H., Mitchell, J., Pallentin, A., Kane, T., Woelz, S., Bowden, D., Rowden, A.A., Pecher, I.A., 2020. Focused fluid seepage related to variations in accretionary wedge structure, hikurangi margin, New Zealand. Geology 48. https://doi.org/10.1130/G46666.1.

Zucker, E., Gvirtzman, Z., Steinberg, J., Enzel, Y., 2020. Salt tectonics in the Eastern Mediterranean Sea: where a giant delta meets a salt giant. Geology. https://doi.org/10.1130/g47031.1.

Zucker, E., Gvirtzman, Z., Steinberg, J., Enzel, Y., 2017. Diversion and morphology of submarine channels in response to regional slopes and localized salt tectonics, Levant Basin. Mar. Petrol. Geol. https://doi.org/10.1016/j.marpetgeo.2017.01.002.